Editors' Suggestion

Hierarchy of Ideal Flatbands in Chiral Twisted Multilayer Graphene Models

Jie Wang[1,*] and Zhao Liu[2,†]

[1]*Center for Computational Quantum Physics, Flatiron Institute, 162 5th Avenue, New York, New York 10010, USA*
[2]*Zhejiang Institute of Modern Physics, Zhejiang University, Hangzhou 310027, China*

(Received 27 September 2021; accepted 24 March 2022; published 29 April 2022)

We propose models of twisted multilayer graphene that exhibit exactly flat Bloch bands with arbitrary Chern numbers and ideal band geometries. The models are constructed by twisting two sheets of Bernal-stacked multiple graphene layers with only intersublattice couplings. Analytically we show that flatband wave functions in these models exhibit a momentum space holomorphic character, leading to ideal band geometries. We also explicitly demonstrate a generic "wave function exchange" mechanism that generates the high Chern numbers of these ideal flatbands. The ideal band geometries and high Chern numbers of the flatbands imply the possibility of hosting exotic fractional Chern insulators which do not have analogues in continuum Landau levels. We numerically verify that these exotic fractional Chern insulators are model states for short-range interactions, characterized by exact ground-state degeneracies at zero energy and infinite particle-cut entanglement gaps.

DOI: 10.1103/PhysRevLett.128.176403

Introduction.—The intrinsic topological and geometric properties of Bloch wave functions are crucial to the interacting phenomena in narrow-band systems such as moiré materials [1–3] where the electrons' kinetic energies are quenched. The band topology enriches the possible many-body phase diagram [4–6]. On the other hand, the band geometry determines the actual stabilities of various many-body states [7].

As a representative example, twisted bilayer graphene (TBG) has two nearly flatbands of Chern number $\mathcal{C} = \pm 1$ at charge neutrality. Recently, fractional Chern insulators (FCIs) [4–6] were theoretically predicted and experimentally observed in TBG flatbands [8–11]. One important factor to the stability of FCIs in this system is due to the ideal geometry of the flatbands in the fixed point chiral limit [12,13], where each flatband's Berry curvature $\Omega_{\boldsymbol{k}}$ is nonvanishing and strictly proportional to its Fubini-Study metric $g^{ab}_{\boldsymbol{k}}$ by a constant determinant-one matrix ω^{ab} [14–16]:

$$g^{ab}_{\boldsymbol{k}} = \frac{1}{2}\omega^{ab}\Omega_{\boldsymbol{k}}, \qquad \Omega_{\boldsymbol{k}} \neq 0 \quad \text{for} \quad \forall\ \boldsymbol{k}, \tag{1}$$

where $a, b = x, y$ labels spatial coordinates. The ideal band geometry Eq. (1) implies the Bloch wave functions of the chiral TBG (CTBG) flatbands exhibit a momentum space holomorphic character [17,18], in analogy to the real space holomorphic wave function in the conventional lowest Landau level (LLL). Such exact position-momentum duality leads to the existence of model FCIs in the CTBG flatbands as the exact zero-energy ground states of short-range interactions which are stable against the spatial fluctuation of band geometries [14,16].

The ideal flatbands are special cases of the Kähler band [19–21] when the Kähler structure [22] is spatially constant. There is so far a glaring lack of microscopic models realizing ideal flatbands of high Chern numbers (high-$\mathcal{C}$). Compared with $|\mathcal{C}| = 1$ bands, high-$\mathcal{C}$ bands are topologically different [23–25] and may support many-body phases without LL analogues [26–34]. In this work, we fill this void and propose a systematic construction of microscopic models with relevance to moiré materials. Our models are based on two sheets of n-layer Bernal stacked graphene which are twisted by a small angle and put in the chiral limit. Our hierarchy scheme starts with CTBG as the parent, and includes the chiral twisted double bilayer graphene (CTDBG) as the next descendant [35–43]. We show exactly flat bands existing at charge neutrality of our models, and we analytically and mathematically prove their ideal band geometry and exotic band topology. We also numerically show that lattice-specific FCIs without LLL analogues are stable in these ideal flatbands as they appear as the exact zero-energy ground states of short-range interactions, paving the way towards understanding their stability against inhomogeneous band geometries.

Multilayer chiral model.—We consider two sheets of n-layer Bernal stacked graphene twisted by a small angle θ, as illustrated in Fig. 1. We focus on a single valley of the system [44–46] and take the chiral limit [12] by keeping only the intersublattice hopping between adjacent layers, such that the Hamiltonian of our model takes an off-diagonal form in the sublattice basis

$$H_n = (\Phi^\dagger \quad \Xi^\dagger)\begin{pmatrix} & \mathcal{D}_n \\ \mathcal{D}_n^\dagger & \end{pmatrix}\begin{pmatrix} \Phi \\ \Xi \end{pmatrix}, \tag{2}$$

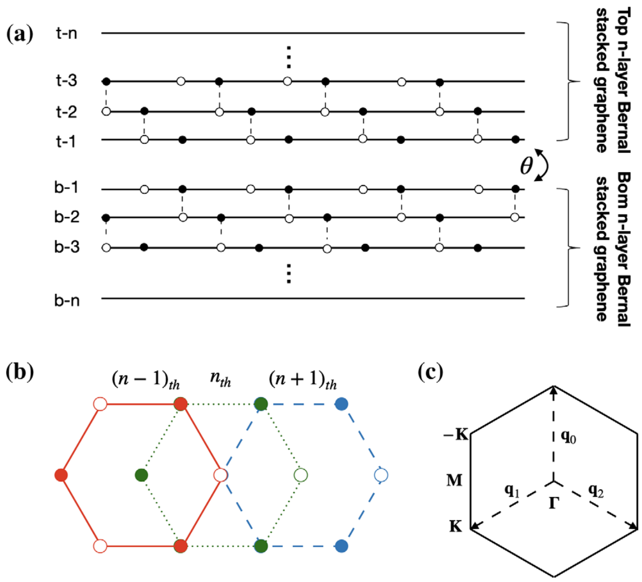

FIG. 1. (a) Geometry of our *AB*-*AB* Bernal stacking multilayered model, which consists of n layers of Bernal stacked graphene on top and bottom sheets, respectively, with a relative small twisted angle θ in the middle. Here the solid and empty dots represent the A and B sublattice, respectively. (b) Illustration of the Bernal stacking structure in three consecutive layers. (c) The moiré Brillouin zone and some important momentum points.

where the basis Φ and Ξ are fully sublattice-A and B polarized. We organize Φ (and Ξ) by layers, such that $\Phi = (\phi_1, \phi_2, \ldots, \phi_n)^T$ where $\phi_i = (\phi_i^b, \phi_i^t)^T$ contains the sublattice-A components of the ith layer in the bottom sheet and the ith layer in the top sheet (Fig. 1). In this basis, we have

$$\mathcal{D}_n = \begin{pmatrix} \mathcal{D}_1 & t_1 T_+ & & & & \\ t_1 T_- & h_D & t_2 T_+ & & & \\ & t_2 T_- & h_D & \ddots & & \\ & & \ddots & & & \\ & & & & & t_{n-1} T_+ \\ & & & & t_{n-1} T_- & h_D \end{pmatrix},$$

where h_D and $\mathcal{D}_1$ are, respectively, the Dirac Hamiltonian of a freestanding monolayer graphene and the Hamiltonian of CTBG [12], given by

$$h_D = \begin{pmatrix} -i\partial & \\ & -i\partial \end{pmatrix}, \qquad \mathcal{D}_1 = \begin{pmatrix} -i\partial & U_{-\phi} \\ U_{\phi}^* & -i\partial \end{pmatrix}. \tag{3}$$

Here $U_\phi = \alpha(e^{-i\boldsymbol{q}_0\cdot\boldsymbol{r}} + e^{i\phi}e^{-i\boldsymbol{q}_1\cdot\boldsymbol{r}} + e^{-i\phi}e^{-i\boldsymbol{q}_2\cdot\boldsymbol{r}})$ with $\phi = 2\pi/3$ and $\alpha \propto \sin^{-1}(\theta/2)$ [12], $\partial = (\partial_x - i\partial_y)/\sqrt{2}$, and the momenta $\boldsymbol{q}_{0,1,2}$ are illustrated in Fig. 1(c). The twist angle θ is set as the magic angle of CTBG [12]. We only retain the strongest tunneling in the Bernal stacking structure [Fig. 1(b)], which couples electrons in the nth layer sublattice A to those in the $(n+1)$th layer sublattice B by the real tunneling strength t_n [Fig. 1(a)]. Under this assumption, the interlayer coupling matrices $T_\pm$ are

$$T_+ = \begin{pmatrix} 1 & 0 \\ 0 & 0 \end{pmatrix}, \qquad T_- = \begin{pmatrix} 0 & 0 \\ 0 & 1 \end{pmatrix}. \tag{4}$$

Details of the model Hamiltonian are left to the Supplemental Material (SM) [47].

The model Eq. (2) preserves the translation $\mathcal{V}_{1,2}$ and the threefold rotation $\mathcal{C}_3$ symmetries, but it breaks the time-reversal $\mathcal{T}$ and the twofold rotation $\mathcal{C}_2$ as they interchange valleys [48–52]. The combination $\mathcal{C}_2\mathcal{T}$ is also broken by the Bernal stacking unless $n = 1$. Besides the lattice symmetries, the model has two exact emergent symmetries: the chiral symmetry σ_z and the intravalley inversion symmetry $\mathcal{I}$. As defined in Table I, they respectively imply a particle-hole symmetry and an inversion symmetry to the spectrum and eigen-wave-function. In the definition of $\mathcal{I}$, $\mathcal{K}$ is the complex conjugation operator and $\mathcal{P} = \mathrm{diag}[\tau_y, -\tau_y, \ldots, (-)^{n-1}\tau_y]$, where τ_y acts on the ith bottom and top layers. Throughout this work, we use Pauli matrix $\boldsymbol{\sigma}$ for sublattice and $\boldsymbol{\tau}$ for layers. Note that the intravalley inversion $\mathcal{I}$ reduces to the known form for CTBG [15] when the $\mathcal{C}_2\mathcal{T}$ symmetry is restored [53]. Ignoring the negligible small twist angle effect, $\mathcal{I}$ is identical to the approximate unitary particle-hole symmetry [51,54–59].

Twisted bilayer graphene.—We now proceed to demonstrate the existence of ideal flatbands in our model. For the simplest case $n = 1$ CTBG, Refs. [12,14,15,60–64] show that it is an exactly solvable model exhibiting $|\mathcal{C}| = 1$ dispersionless bands at charge neutrality with ideal band geometry at magic angles. Its wave function has an exact representation [15] (up to normalization) in terms of the LLL wave function $\Phi_{\boldsymbol{k}}^{\mathrm{LLL}}(\boldsymbol{r})$ [65–68]:

TABLE I. Exact emergent symmetries of the model, which include the chiral symmetry σ_z and the intravalley inversion symmetry $\mathcal{I}$. The combination of both symmetries implies that the spectrum is not only particle-hole symmetric but also $\boldsymbol{k}$ to $-\boldsymbol{k}$ symmetric within the same valley. The matrices above are written in the sublattice basis Φ and Ξ.

Chiral symmetry	Intravalley inversion symmetry
$\sigma_z = \begin{pmatrix} 1 & \\ & -1 \end{pmatrix}$	$\mathcal{I} = \begin{pmatrix} \mathcal{P} & \\ & -\mathcal{P} \end{pmatrix}\sigma_x\mathcal{K}$
$\{H, \sigma_z\} = 0$	$[H, \mathcal{I}] = 0$

$$\Phi_1 = \begin{pmatrix} \phi_1 \\ \phi_1' \end{pmatrix} = \begin{pmatrix} i\mathcal{G}(\boldsymbol{r}) \\ \eta\mathcal{G}(-\boldsymbol{r}) \end{pmatrix} \Phi_{\boldsymbol{k}}^{\mathrm{LLL}}(\boldsymbol{r}), \tag{5}$$

where $\eta = \pm 1$ is the intravalley inversion eigenvalue and the $\boldsymbol{k}$-independent $\mathcal{G}(\boldsymbol{r})$ can be interpreted as a quantum Hall wave function in a magnetic field oppositely directed to that of $\Phi_{\boldsymbol{k}}^{\mathrm{LLL}}(\boldsymbol{r})$ [15]. This connection to the LLL wave function implies that its cell periodic wave function $e^{-i\boldsymbol{k}\cdot\boldsymbol{r}}\Phi_{1,\boldsymbol{k}}$ is holomorphic in $k = (k_x + ik_y)/\sqrt{2}$ ignoring the normalization factor [69]. For any Bloch wave function satisfying this property, Eq. (1) is automatically satisfied [14,16,17,70]. The unit Chern number and ideal band geometry thereby make CTBG an exact $\boldsymbol{k}$-space dual of the LLL with nontrivial curvature [16].

Twisted double bilayer graphene.—We now discuss the first nontrivial case, i.e., $n = 2$ CTDBG. It has been noticed that CTDBG has two exactly flat bands at charge neutrality [37]. Despite this observation, the wave function, topology, and geometry of these flatbands were ignored before, which we will analyze in detail below. Since the two flatbands are sublattice polarized and related by $\mathcal{I}$, without loss of generality we focus on the sublattice-A flatband wave function Φ_2 which is the zero mode of $\mathcal{D}_2^\dagger$. We denote Φ_2 as $(\tilde{\Phi}_1^T, \phi_2, \phi_3)^T$ where $\tilde{\Phi}_1 = (\tilde{\phi}_1, \tilde{\phi}_1')^T$ is a two-component layer spinor. Component-wisely, the zero mode equation $\mathcal{D}_2^\dagger \Phi_2 = 0$ becomes

$$\mathcal{D}_1^\dagger \tilde{\Phi}_1 + t_1(0, \phi_3)^T = 0, \qquad -i\bar{\partial}\phi_3 = 0, \tag{6}$$

$$-i\bar{\partial}\phi_2 + t_1\tilde{\phi}_1 = 0. \tag{7}$$

The solutions of these equations are $\phi_3 = 0$ [71] and $\tilde{\Phi}_1$ being annihilated by $\mathcal{D}_1^\dagger$. So $\tilde{\Phi}_1$ is identical to the CTBG wave function up to a normalization factor: $\tilde{\Phi}_1 = N_{\boldsymbol{k}}\Phi_1$. For $N_{\boldsymbol{k}} \neq 0$ one can rescale Φ_2, so we replace $\tilde{\Phi}_1$ by Φ_1 in below. As only $\mathcal{D}_1^\dagger$ depends on the twist angle, the magic angles of CTDBG and CTBG are identical, at which the bands at charge neutrality are exactly flat.

The only nontrivial zero mode equation for CTDBG is Eq. (7) which governs the essential properties of band topology, band geometry, and interacting physics through ϕ_2. To prove the ideal band geometry of the magic angle CTDBG, we merely need to show the cell-periodic part of ϕ_2 ($u_{1,2} \equiv e^{-i\boldsymbol{k}\cdot\boldsymbol{r}}\phi_{1,2}$) is holomorphic in k up to a normalization, since Φ_1, as the zero mode of CTBG, is already proved to satisfy this condition [14]. The key observation is that Eq. (7) only has antiholomorphic derivative $\bar{\partial}$, thereby the differential equation for u_2, $(\bar{\partial} + ik)u_2 = -it_1u_1$, depends only on k but not on $\bar{k}$. Then $\bar{\partial}_k u_2 = 0$ follows immediately from the fact that $\bar{\partial}_k u_1 = 0$. At momentum points where $N_{\boldsymbol{k}} = 0$, the zero mode equation $(\bar{\partial} + ik)u_2 = 0$ also immediately implies the $\boldsymbol{k}$-space holomorphic property of u_2 and thus the ideal band geometry of Φ_2.

Next we discuss band topology. While it is known that the Bernal-stacking structure can support high Chern number [37,72,73], here we provide a proof which highlights the analytical structure of the CTDBG flatband wave function. For convenience, in the following we assume a small hexagonal-boron-nitride potential $\mu > 0$ to split the degeneracy of the two CTDBG flatbands and meanwhile preserve their sublattice polarization.

We start by considering the limit of zero interlayer coupling $t_1 = 0$. In this case, in the low-energy regime there are two exactly flat bands $(\phi_{\mathrm{CTBG}}, \chi_{\mathrm{CTBG}})$ originating from the inner CTBG layers and two Dirac bands (ϕ_D, χ_D) from the outermost layers. The CTBG and the Dirac bands are degenerate at the Dirac points $\pm\boldsymbol{K}$, as shown in Fig. 2(a). In the following, we focus on the Dirac point $\boldsymbol{K}$ to examine the gap opening mechanism as the physics at $-\boldsymbol{K}$ is simply implied by the intravalley inversion. The $\boldsymbol{K}$ point wave functions $(\phi_{\mathrm{CTBG}}, \phi_D)$ at energy μ are sublattice-A polarized and $(\chi_{\mathrm{CTBG}}, \chi_D)$ at energy $-\mu$ are sublattice-B polarized [Fig. 2(a)]. We further note that (ϕ_D, χ_D) are also polarized in the bottom layer. Under this scenario, in the "(bottom, top)" layer basis we have

$$\begin{aligned} \phi_{\mathrm{CTBG}} &= (\phi_1, \phi_1')^T, \qquad \phi_D = (1,0)^T, \\ \chi_{\mathrm{CTBG}} &= (\chi_1, \chi_1')^T, \qquad \chi_D = (1,0)^T. \end{aligned} \tag{8}$$

We then turn on an infinitesimal t_1 and use the perturbation theory to study the change of band structure and wave functions. As the t_1 terms couple adjacent layers of opposite sublattices, the perturbation matrix elements within the four low-energy bands are

$$\langle \phi_{\mathrm{CTBG}} | T_+ | \chi_D \rangle \neq 0, \qquad \langle \chi_{\mathrm{CTBG}} | T_- | \phi_D \rangle = 0, \tag{9}$$

where details of Eq. (8) and Eq. (9) can be found in the SM.

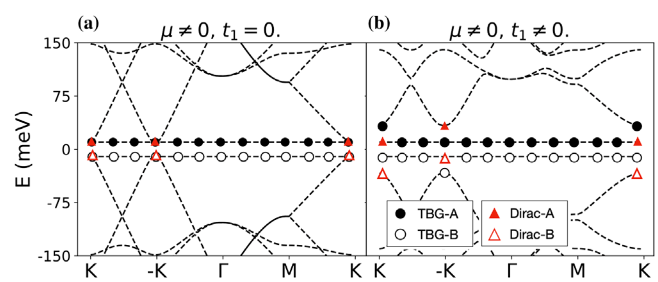

FIG. 2. High-$\mathcal{C}$ bands generated by the "wave function exchange" mechanism. In (a) and (b), we show the sublattice polarization properties of the CTBG (black circles) and Dirac wave functions (red triangles) before and after turning on an infinitesimal interlayer coupling t_1, respectively, where the solid (empty) markers represent sublattice-A (B) polarization, respectively. The Dirac wave function interchanges with the CTBG wave function at $\pm\boldsymbol{K}$, which punctures a zero to CTBG wave function and increases the Chern number by one.

Equation (9) implies that χ_{CTBG} and ϕ_D are unperturbed at $\boldsymbol{K}$, but ϕ_{CTBG} and χ_D start to repel each other immediately after turning on t_1. The net result is that a band gap is opened and the CTBG and Dirac bands at positive energy are effectively "exchanged" at $\boldsymbol{K}$ [Fig. 2(b)], leaving $\Phi_{2,\boldsymbol{K}}$ to be $(0,0,1,0)^T$. We find that $\Phi_{2,\boldsymbol{K}}$ remains $(0,0,1,0)^T$ for arbitrary $t_1 \neq 0$ because the flatband energy stays at μ independent of t_1. On the other hand, Eq. (6) dictates that first two components of Φ_2 are identical to the CTBG wave function up to a normalization factor $N_{\boldsymbol{k}}$. Thus our analysis shows $N_{\boldsymbol{k}}$ must be zero at $\boldsymbol{K}$; how fast $N_{\boldsymbol{k}}$ decays to zero when $\boldsymbol{k}$ approaching $\boldsymbol{K}$ is determined by $|t_1|$.

This "wave function exchange" increases the flatband Chern number by one. The Chern number measures the discontinuity of the Bloch wave function which resides either at the boundary or in the bulk of the Brillouin zone [74,75]. Since $\mathcal{C}$ is an invariant, it is sufficient to work with an infinitesimal $|t_1|$. In this case, the CTDBG wave function is identical to the CTBG wave function except near the Dirac points. One can choose the Brillouin zone boundary to avoid the Dirac points such that the boundary contribution to $\mathcal{C}$ is determined by CTBG wave function which equals to one. The vanishing of $N_{\boldsymbol{K}}$ is equivalent as stating a pole singularity of the Dirac component ϕ_D at $\boldsymbol{K}$, which increases the Chern number by one following Refs. [17,18]. We therefore proved the CTDBG flatband has Chern number two.

Hierarchy scheme.—The discussion of CTDBG ($n=2$) can be straightforwardly generalized to arbitrary n. Given the zero mode wave function Φ_{n-1} of H_{n-1}, the zero mode of H_n must exist at the same magic angle, whose ansatz can be written as $\Phi_n^T = (\Phi_{n-1}^T, \phi_n, 0)$ and the zero-mode equation generalizing Eq. (7) is

$$-i\bar{\partial}\phi_n + t_{n-1}\phi_{n-1} = 0. \tag{10}$$

Since Eq. (10) only has antiholomorphic derivatives, the cell-periodic part of ϕ_n is a holomorphic function of k as that of ϕ_{n-1} is. We therefore prove the ideal band geometry of Φ_n from the hierarchy construction. The band topology can also be analyzed by the same method. Starting with $t_{n-1}=0$, $t_{i=1,\ldots,n-2} \neq 0$, the H_n at the magic angle consists of two sublattice polarized flatbands originating from Φ_{n-1} which are degenerate with the two outermost freestanding Dirac bands at Dirac points. Finite but infinitesimal $|t_{n-1}|$ splits the degeneracy and "exchanges" the Φ_{n-1} with the Dirac band leaving $\Phi_{n,\boldsymbol{K}}$ to be $(0,\ldots,0,1,0)^T$. This does not alter the boundary contribution to $\mathcal{C}$ but generates an unavoidable bulk pole singularity and increases $\mathcal{C}$ by one. We therefore prove the Chern number of our flatband equals to the number of layers and all the flatbands have ideal band geometry satisfying Eq. (1). These results do not require infinitesimal $t_{i=1,\ldots,n}$, because Chern number is a topological invariant and the ideal geometry follows directly from the holomorphic property of the zero-mode equations.

Exact fractional Chern insulators.—We now examine the interacting physics in the ideal flatband of our model. As the pertinent band is exactly flat, we drop the kinetic energy and project the interaction into the ideal flatband. The band filling factor ν is defined as $N/(N_1N_2)$ for N electrons and N_1, N_2 unit cells in the two primitive directions of the moiré pattern. As the many-body Hamiltonian preserves the total momentum, each eigenstate can be labeled by its total momentum (K_1, K_2). In TBG, it has been numerically demonstrated that the $\mathcal{C}=1$ flatband at the charge neutrality can host the lattice Laughlin FCIs at $\nu = 1/3$ [8–10]. In particular, the model $\nu=1/3$ Laughlin state was found to be the exact zero-energy ground state at the chiral limit for the short-ranged two-body repulsive interaction $H_{\mathrm{int}} = \sum_{i<j} \delta''(\boldsymbol{r}_i - \boldsymbol{r}_j)$ [76].

In high-$\mathcal{C}$ Bloch bands, robust FCIs were reported across various models [26–34]. Remarkably, in our ideal flatbands, we observe *exact* $(2n+1)$-fold degenerate zero-energy ground states for H_{int}, separated by a finite energy gap to excitations [Figs. 3(a) and 3(b) for $n=2$ and $n=3$]. Their particle-cut entanglement spectra (PES) [4], defined

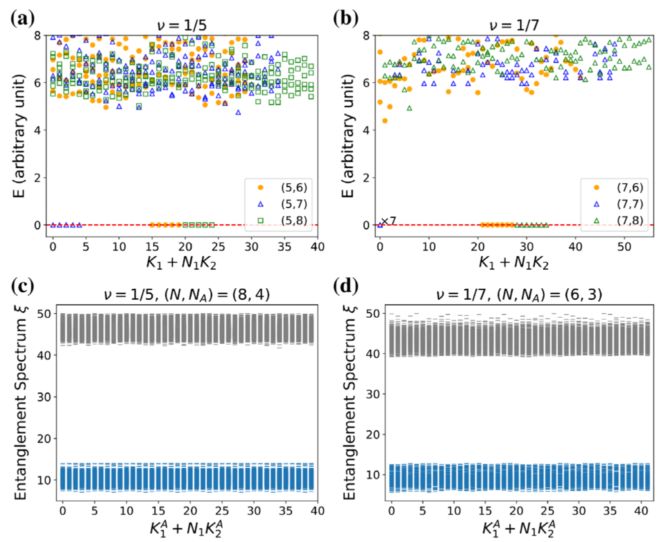

FIG. 3. Energy spectra and particle-cut entanglement spectra (PES) demonstrating exact model FCIs. (a) and (b): Energy spectra of the repulsive interaction $H_{\mathrm{int}} = \sum_{i<j} \delta''(\boldsymbol{r}_i - \boldsymbol{r}_j)$ in the $\mathcal{C}=n$ ideal flatband at filling fraction $\nu = 1/(2n+1)$, where (a) is for $n=2$ (CTDBG) and (b) is for $n=3$ (chiral twisted double trilayer graphene, CTDTG). An $(2n+1)$-fold exactly degenerate ground states at zero energy are clearly observed. Lattice sizes $(N_1, N_2) = (2n+1, N)$ are given in the legends. The red dashed lines mark the zero energy and are used to guide the eyes. (c) and (d): PES for $N=8$ and $N=6$ particles. The grey levels above $\xi_c = |\ln(2^{-53})| \approx 36.7$ are machine noises. The number of low-energy PES levels is 17710 and 3248 in (c) and (d) respectively, agreeing with the FCI quasihole counting [26,27].

as the entanglement between subsystems of N_A and $N - N_A$ particles, are displayed in Figs. 3(c) and 3(d). The counting of low PES levels agrees with the expectation from FCI quasihole excitations. The high PES levels appear only above the machine error cutoff $\xi_c \approx 36.7$, strongly suggesting an infinite PES gap and the exact zero modes are model FCIs. See the SM for studies away from the chiral limit.

Discussions.—There are a couple of open questions which deserve future studies. We noticed that the model FCIs are intrinsic to the outermost Dirac layer: further projecting H_{int} into the ϕ_n component of Φ_n changes the energies of excited states but leaves the exact degenerate zero-energy ground states and the PES unaffected. This means ϕ_n alone could exhibit a "color-entangled" feature [28] which remains challenging to uncover analytically from the zero mode equation Eq. (10). Furthermore, a thorough understanding of the origin of the exact model FCIs is still lacking. Exact model FCIs were also reported in the numerical studies of onsite interacting bosons in the Kapit-Mueller model [77,78] and its variations [31]. Considering the band geometry of the Kapit-Mueller model is also ideal [79], we anticipate the ideal geometry is the fundamental origin of the frustration free nature of these lattice-specific interacting Hamiltonians. Studying the projected density algebra is an interesting future direction [80–84].

J. W. is grateful to Bartholomew Andrews, Semyon Klevtsov, Nicolas Regnault, and Ya-Hui Zhang for useful discussions. We acknowledge Jennifer Cano, Andrew J. Millis, and Bo Yang for the collaboration on Ref. [16]. Z. L. acknowledges Ahmed Abouelkomsan and Emil J. Bergholtz for the collaboration on related topics. Z. L. is supported by the National Key Research and Development Program of China through Grant No. 2020YFA0309200. The Flatiron Institute is a division of the Simons Foundation. The authors are grateful to Lucy Reading-Ikkanda for creating the cover figure.

Note added.—Recently, Ref. [85] appeared, which overlaps with the results reported here.

*jiewang@flatironinstitute.org
†zhaol@zju.edu.cn

[1] E. Y. Andrei and A. H. MacDonald, Nat. Mater. **19**, 1265 (2020).
[2] L. Balents, C. R. Dean, D. K. Efetov, and A. F. Young, Nat. Phys. **16**, 725 (2020).
[3] D. M. Kennes, M. Claassen, L. Xian, A. Georges, A. J. Millis, J. Hone, C. R. Dean, D. N. Basov, A. N. Pasupathy, and A. Rubio, Nat. Phys. **17**, 155 (2021).
[4] N. Regnault and B. A. Bernevig, Phys. Rev. X **1**, 021014 (2011).
[5] S. A. Parameswaran, R. Roy, and S. L. Sondhi, C.R. Phys. **14**, 816 (2013).
[6] E. J. Bergholtz and Z. Liu, Int. J. Mod. Phys. B **27**, 1330017 (2013).
[7] T. S. Jackson, G. Möller, and R. Roy, Nat. Commun. **6**, 8629 (2015).
[8] A. Abouelkomsan, Z. Liu, and E. J. Bergholtz, Phys. Rev. Lett. **124**, 106803 (2020).
[9] C. Repellin and T. Senthil, Phys. Rev. Research **2**, 023238 (2020).
[10] C. Repellin, Z. Dong, Y.-H. Zhang, and T. Senthil, Phys. Rev. Lett. **124**, 187601 (2020).
[11] Y. Xie, A. T. Pierce, J. M. Park, D. E. Parker, E. Khalaf, P. Ledwith, Y. Cao, S. H. Lee, S. Chen, P. R. Forrester, K. Watanabe, T. Taniguchi, A. Vishwanath, P. Jarillo-Herrero, and A. Yacoby, Nature (London) **600**, 439 (2021).
[12] G. Tarnopolsky, A. J. Kruchkov, and A. Vishwanath, Phys. Rev. Lett. **122**, 106405 (2019).
[13] O. Vafek and J. Kang, Phys. Rev. Lett. **125**, 257602 (2020).
[14] P. J. Ledwith, G. Tarnopolsky, E. Khalaf, and A. Vishwanath, Phys. Rev. Research **2**, 023237 (2020).
[15] J. Wang, Y. Zheng, A. J. Millis, and J. Cano, Phys. Rev. Research **3**, 023155 (2021).
[16] J. Wang, J. Cano, A. J. Millis, Z. Liu, and B. Yang, Phys. Rev. Lett. **127**, 246403 (2021).
[17] M. Claassen, C. H. Lee, R. Thomale, X.-L. Qi, and T. P. Devereaux, Phys. Rev. Lett. **114**, 236802 (2015).
[18] C. H. Lee, M. Claassen, and R. Thomale, Phys. Rev. B **96**, 165150 (2017).
[19] T. Ozawa and B. Mera, Phys. Rev. B **104**, 045103 (2021).
[20] B. Mera and T. Ozawa, Phys. Rev. B **104**, 045104 (2021).
[21] B. Mera and T. Ozawa, Phys. Rev. B **104**, 115160 (2021).
[22] M. R. Douglas and S. Klevtsov, Commun. Math. Phys. **293**, 205 (2010).
[23] M. Trescher and E. J. Bergholtz, Phys. Rev. B **86**, 241111 (R) (2012).
[24] S. Yang, Z.-C. Gu, K. Sun, and S. Das Sarma, Phys. Rev. B **86**, 241112(R) (2012).
[25] A. Kruchkov, arXiv:2105.14672.
[26] Z. Liu, E. J. Bergholtz, H. Fan, and A. M. Läuchli, Phys. Rev. Lett. **109**, 186805 (2012).
[27] A. Sterdyniak, C. Repellin, B. A. Bernevig, and N. Regnault, Phys. Rev. B **87**, 205137 (2013).
[28] Y.-L. Wu, N. Regnault, and B. A. Bernevig, Phys. Rev. Lett. **110**, 106802 (2013).
[29] G. Möller and N. R. Cooper, Phys. Rev. Lett. **115**, 126401 (2015).
[30] Y.-H. Wu, J. K. Jain, and K. Sun, Phys. Rev. B **91**, 041119 (R) (2015).
[31] J. Behrmann, Z. Liu, and E. J. Bergholtz, Phys. Rev. Lett. **116**, 216802 (2016).
[32] B. Andrews and G. Möller, Phys. Rev. B **97**, 035159 (2018).
[33] B. Andrews, T. Neupert, and G. Möller, Phys. Rev. B **104**, 125107 (2021).
[34] B. Andrews, M. Mohan, and T. Neupert, Phys. Rev. B **103**, 075132 (2021).
[35] M. Koshino, Phys. Rev. B **99**, 235406 (2019).
[36] J. A. Crosse, N. Nakatsuji, M. Koshino, and P. Moon, Phys. Rev. B **102**, 035421 (2020).
[37] F. Haddadi, Q. Wu, A. J. Kruchkov, and O. V. Yazyev, Nano Lett. **20**, 2410 (2020).
[38] J. Y. Lee, E. Khalaf, S. Liu, X. Liu, Z. Hao, P. Kim, and A. Vishwanath, Nat. Commun. **10**, 5333 (2019).

[39] Z. Liu, A. Abouelkomsan, and E. J. Bergholtz, Phys. Rev. Lett. **126**, 026801 (2021).

[40] Y. Shi, S. Xu, Y. Yang, S. Slizovskiy, S. V. Morozov, S.-K. Son, S. Ozdemir, C. Mullan, J. Barrier, J. Yin, A. I. Berdyugin, B. A. Piot, T. Taniguchi, K. Watanabe, V. I. Fal'ko, K. S. Novoselov, A. K. Geim, and A. Mishchenko, Nature (London) **584**, 210 (2020).

[41] F. R. Geisenhof, F. Winterer, A. M. Seiler, J. Lenz, T. Xu, F. Zhang, and R. T. Weitz, Nature (London) **598**, 53 (2021).

[42] F. Zhang, J. Jung, G. A. Fiete, Q. Niu, and A. H. MacDonald, Phys. Rev. Lett. **106**, 156801 (2011).

[43] J. Jung and A. H. MacDonald, Phys. Rev. B **89**, 035405 (2014).

[44] R. Bistritzer and A. H. MacDonald, Proc. Natl. Acad. Sci. U.S.A. **108**, 12233 (2011).

[45] J. M. B. Lopes dos Santos, N. M. R. Peres, and A. H. Castro Neto, Phys. Rev. B **86**, 155449 (2012).

[46] J. M. B. Lopes dos Santos, N. M. R. Peres, and A. H. Castro Neto, Phys. Rev. Lett. **99**, 256802 (2007).

[47] See Supplemental Material at http://link.aps.org/supplemental/10.1103/PhysRevLett.128.176403 for more details on the band geometry, band topology and interacting physics of our models.

[48] E. J. Mele, Phys. Rev. B **84**, 235439 (2011).

[49] H. C. Po, L. Zou, A. Vishwanath, and T. Senthil, Phys. Rev. X **8**, 031089 (2018).

[50] L. Zou, H. C. Po, A. Vishwanath, and T. Senthil, Phys. Rev. B **98**, 085435 (2018).

[51] Z. Song, Z. Wang, W. Shi, G. Li, C. Fang, and B. A. Bernevig, Phys. Rev. Lett. **123**, 036401 (2019).

[52] N. Bultinck, E. Khalaf, S. Liu, S. Chatterjee, A. Vishwanath, and M. P. Zaletel, Phys. Rev. X **10**, 031034 (2020).

[53] Intravalley inversion in Ref. [15] is defined as $\mathcal{I}' \equiv \mathrm{diag}(\mathcal{P}, -\mathcal{P})$ which differs from $\mathcal{I}$ by $\sigma_x\mathcal{K}$, a combination of $\mathcal{C}_2\mathcal{T}$ and $\boldsymbol{r} \to -\boldsymbol{r}$. $\mathcal{C}_2\mathcal{T}$ invariance of H_1 implies $\mathcal{I}' H_1(\boldsymbol{r})\mathcal{I}'^{\dagger} = H_1(-\boldsymbol{r})$ which is consistent with Ref. [15].

[54] B. A. Bernevig, Z.-D. Song, N. Regnault, and B. Lian, Phys. Rev. B **103**, 205411 (2021).

[55] Z.-D. Song, B. Lian, N. Regnault, and B. A. Bernevig, Phys. Rev. B **103**, 205412 (2021).

[56] B. A. Bernevig, Z.-D. Song, N. Regnault, and B. Lian, Phys. Rev. B **103**, 205413 (2021).

[57] B. Lian, Z.-D. Song, N. Regnault, D. K. Efetov, A. Yazdani, and B. A. Bernevig, Phys. Rev. B **103**, 205414 (2021).

[58] B. A. Bernevig, B. Lian, A. Cowsik, F. Xie, N. Regnault, and Z.-D. Song, Phys. Rev. B **103**, 205415 (2021).

[59] F. Xie, A. Cowsik, Z.-D. Song, B. Lian, B. A. Bernevig, and N. Regnault, Phys. Rev. B **103**, 205416 (2021).

[60] S. Becker, M. Embree, J. Wittsten, and M. Zworski, arXiv:2008.08489.

[61] S. Becker, M. Embree, J. Wittsten, and M. Zworski, Phys. Rev. B **103**, 165113 (2021).

[62] Y. Ren, Q. Gao, A. H. MacDonald, and Q. Niu, Phys. Rev. Lett. **126**, 016404 (2021).

[63] F. K. Popov and A. Milekhin, Phys. Rev. B **103**, 155150 (2021).

[64] G. G. Naumis, L. A. Navarro-Labastida, E. Aguilar-Méndez, and A. Espinosa-Champo, Phys. Rev. B **103**, 245418 (2021).

[65] J. Wang, S. D. Geraedts, E. H. Rezayi, and F. D. M. Haldane, Phys. Rev. B **99**, 125123 (2019).

[66] F. D. M. Haldane, J. Math. Phys. (N.Y.) **59**, 071901 (2018).

[67] S. D. Geraedts, J. Wang, E. H. Rezayi, and F. D. M. Haldane, Phys. Rev. Lett. **121**, 147202 (2018).

[68] J. Wang, Phys. Rev. Lett. **122**, 257203 (2019).

[69] Following Refs. [65–68], the LLL wave function $\Phi_{\boldsymbol{k}}^{\mathrm{LLL}}(\boldsymbol{r})$ can be expressed in terms of the modified Weierstrass sigma function $\sigma(z)$ as $e^{ik^* z}\sigma(z + ik)e^{-\frac{1}{2}(|z|^2+|k|^2)}$. Its "cell-periodic" part $u_{\boldsymbol{k}}^{\mathrm{LLL}}(\boldsymbol{r}) \equiv e^{-i\boldsymbol{k}\cdot\boldsymbol{r}}\Phi_{\boldsymbol{k}}^{\mathrm{LLL}}(\boldsymbol{r})$ is holomorphic in k ignoring the normalization factor.

[70] R. Roy, Phys. Rev. B **90**, 165139 (2014).

[71] ϕ_3 cannot be a non-zero constant, which violates the Bloch transnational symmetry.

[72] Y.-H. Zhang, D. Mao, Y. Cao, P. Jarillo-Herrero, and T. Senthil, Phys. Rev. B **99**, 075127 (2019).

[73] J. Liu, Z. Ma, J. Gao, and X. Dai, Phys. Rev. X **9**, 031021 (2019).

[74] D. J. Thouless, J. Phys. C **17**, L325 (1984).

[75] D. J. Thouless, M. Kohmoto, M. P. Nightingale, and M. den Nijs, Phys. Rev. Lett. **49**, 405 (1982).

[76] F. D. M. Haldane, Phys. Rev. Lett. **51**, 605 (1983).

[77] E. Kapit and E. Mueller, Phys. Rev. Lett. **105**, 215303 (2010).

[78] J. Dong and E. J. Mueller, Phys. Rev. A **101**, 013629 (2020).

[79] D. Varjas, A. Abouelkomsan, K. Yang, and E. J. Bergholtz, SciPost Phys. **12**, 118 (2022).

[80] S. M. Girvin, A. H. MacDonald, and P. M. Platzman, Phys. Rev. Lett. **54**, 581 (1985).

[81] S. M. Girvin, A. H. MacDonald, and P. M. Platzman, Phys. Rev. B **33**, 2481 (1986).

[82] F. D. M. Haldane, Phys. Rev. Lett. **107**, 116801 (2011).

[83] C. Repellin, T. Neupert, Z. Papić, and N. Regnault, Phys. Rev. B **90**, 045114 (2014).

[84] E. Dobardžić, M. V. Milovanović, and N. Regnault, Phys. Rev. B **88**, 115117 (2013).

[85] P. J. Ledwith, A. Vishwanath, and E. Khalaf, following Letter, Phys. Rev. Lett. **128**, 176404 (2022).